Progress In Electromagnetics Research C, Vol. 149, 111-121, 2024
PIER C

(Received 7 September 2024, Accepted 22 October 2024, Scheduled 29 October 2024)

Multi-Objective Optimization Design of PMa-BSynRM Rotor Structure Based on Macroscopic Parameters and DPCA

Bo Mao[1], Xiaoyan Diao[1], Huangqiu Zhu[1,*], and Jintao Ju[2]

[1]*School of Electrical and Information Engineering, Jiangsu University, Zhenjiang 212013, China*
[2]*School of Electrical and Information Engineering, Changzhou Institute of Technology, Changzhou 213032, China*

ABSTRACT: The rotor of PMa-BSynRM, with its multi-layer barriers and permanent magnet, poses a challenge in the design process as both torque system and suspension force system performance need to be considered comprehensively. To solve this problem, a multi-objective optimization method for the rotor structure of PMa-BSynRM is proposed in this paper. Firstly, the harmonic characteristics of PMa-BSynRM air gap magnetic field are analyzed based on the magnetic potential and magnetic permeability method. The expression for suspension force under the coupled magnetic field is derived by combining Maxwell tensor method. This analysis reveals the relationship between magnetic field characteristics and suspension force, providing guidance for subsequent optimization design. Secondly, through the analysis of the rotor structure, the macroscopic parameters related to the micro and detailed geometric optimization of the PMa-BSynRM rotor are proposed. Based on these macroscopic parameters, the response surface method and dual-population-based co-evolutionary algorithm (DPCA) are applied to realize a compromise among the optimization objectives. Finally, the proposed optimization method is comprehensively analyzed through simulation analysis and prototype experiment. The simulation and experimental results demonstrate a reduction of 51% in optimized torque ripple and 74% in suspension force ripple, as well as a decrease of 3.2° in the suspension force error angle. After optimization, the performance of the motor torque and suspension force system is significantly improved, thus verifying the effectiveness and superiority of the proposed optimization method.

1. INTRODUCTION

Bearingless motors have received great attention due to the advantages of no friction, no pollution, high reliability, and long service life, so it has broad application prospects in bioengineering, semiconductor industry, aerospace, and other fields [1–3]. In recent years, bearingless motor technology has been developed rapidly, and many traditional motors achieve the function of bearingless motors, such as bearingless permanent magnet synchronous motor (BPMSM), bearingless synchronous reluctance motor (BSynRM), and bearingless induction motor (BIM) [4–6]. PMa-BSynRM inherits the advantages of permanent magnet assisted synchronous reluctance motor and bearingless motor (PMa-SynRM) [7]. Not only can it make full use of the reluctance torque, has high power factor and power density, but also has the advantages of no friction and wear, low vibration and noise.

However, similar to the PMa-SynRM motor, the complex rotor structure of multi-layer barriers and permanent magnets poses a major design challenge. For PMa-SynRM, the research focus of this kind of motor is to optimize the magnetic field distribution by changing the structure of the rotor, and then weaken the torque ripple to make the torque output stable. In [8], the torque ripple reduction methods are proposed with the asymmetric rotor and shifted end-slots. In [9, 10], a comprehensive design procedure is proposed, and the nonlinear behaviors of the rotor iron ribs and the effect of the permanent magnets on the structural design are all taken into account with the proposed iterative design procedure targeting the achievement of a desired power factor.

For PMa-BSynRM, although the rotor structure is similar to PMa-SynRM, some design concepts can be borrowed. However, for PMa-BSynRM, the influence of rotor structure on suspension performance must be considered in the design process, which puts forward more requirements for design. In addition, the influence of the rotor structure on the torque system is sometimes contradictory with that on the suspension force system, so it is necessary to use the multi-objective optimization theory to design the PMa-BSynRM.

At present, the commonly used multi-objective optimization algorithms for motors can be divided into the Taguchi optimization method [11], finite element model (FEM) based search algorithm [12], and surrogate model based search algorithm [13]. Taguchi optimization method is an optimization method based on orthogonal experiment and signal to noise ratio. The principle of the Taguchi method is that an orthogonal experiment is designed, and the best combination of design parameters is selected according to the experimental results. However, the Taguchi optimization method is a local optimization algorithm, and the search value is the local optimal value rather than the global optimal value, so it has a high requirement for the experience of motor design.

Finite element analysis (FEA) is the most popular numerical analysis method, which can be used to establish accurate motor models. It is a very effective multiobjective optimization

---

* Corresponding author: Huangqiu Zhu (zhuhuangqiu@ujs.edu.cn).

doi:10.2528/PIERC24090704

Published by THE ELECTROMAGNETIC ACADEMY

method by combining FEA with an intelligent optimization algorithm, that is, the FEM call is inserted in the intelligent optimization process, and constraints are calculated by a computer script. Genetic algorithm (GA), particle swarm optimization (PSO) and their multi-objective versions, fast non-dominated sorting genetic algorithm (NSGA-II), and multi-objective particle swarm optimization (MOPSO) are often applied to machine optimization. The problem with this approach is that the entire optimization process is a computationally challenging task owing to massive function evaluations based on FEM calls. Hence, an indirect optimization method known as a surrogate model is used, that is, through a small amount of finite element data, a mathematical model can be fitted to the FEM. The commonly used surrogate models include response surface model (RSM) [14, 15], Kriging model [16, 17], radial basis function model [18], etc.

At present, the research of multi-objective optimization design largely relies on computing technology to obtain the optimal design, which provides a large number of design schemes to choose from through the combination and calculation of many parameters. While optimal design can be achieved, the correlation between design parameters and performance enhancement mechanisms is often ignored, resulting in a reliance on the inherent level of computing power to efficiently obtain multi-objective optimization results. Therefore, it is necessary to study the multi-objective optimization of motor from the perspective of performance generating mechanism, so as to provide effective guidance for optimal design and achieve satisfactory design efficiency.

The primary innovation that this paper lies is the impact of PMa-BSynRM air gap magnetic field harmonics on suspension performance, while identifying the specific harmonic order that influences suspension force performance. By designing the parameters of the rotor structure, the concept of macroscopic parameters is proposed, which makes the physical meaning of parameters clearer and simplifies the initial design. Combining the advantages of NSGA-II and MOPSO algorithms a multi-objective optimization method of DPCA is proposed.

The remainder of the paper is organized as follows. In Section 2, the basic structure of PMa-BSynRM and the mathematical model of suspension force are introduced, and the influence of harmonic magnetic field on the performance of suspension force is analyzed. The macroscopic parameter design method and multi-objective optimization method based on RSM and DPCA are presented in Section 3. In Section 4, the proposed optimization method is verified by FEA method and prototype experiment. In Section 5, the conclusion is drawn.

2. MOTOR STRUCTURE AND OPERATION MODEL

2.1. Structure of the PMa-BSynRM

The three-dimensional finite element model of the PMa-BSynRM motor and the two-dimensional cross-section of the stator and rotor are shown in Fig. 1. PMa-BSynRM is mainly composed of stator, rotor, permanent magnet, torque winding, and suspension force winding. There are two sets of windings in the stator slot, the torque winding with pole pairs $p_m = 2$ and suspension winding with pole pairs $p_s = 1$. The rotor is a three-layer U-shaped barrier structure with a rib in the middle of the barrier to enhance the rotor strength. Permanent magnets are embedded in the barrier to assist excitation to improve the power factor and power density of the motor.

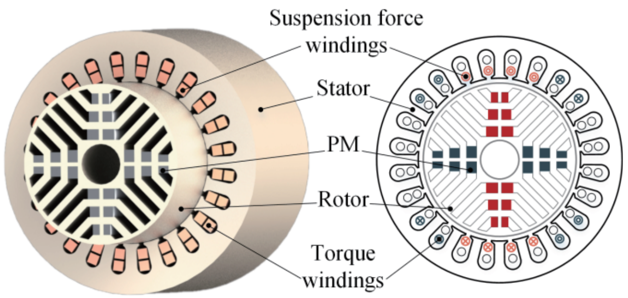

FIGURE 1. Topology of the PMa-BSynRM.

2.2. Modeling of the Suspension Force

For PMa-BSynRM, when the number of poles of torque winding and suspension force winding meets the requirements, and the current frequencies of torque winding and suspension force winding are the same, the stable suspension force with controllable direction can be obtained by controlling the current phase of suspension winding. The following is a further explanation of the suspension principle of PMa-BSynRM combined with the mathematical model of suspension force.

The air gap magnetic field of PMa-BSynRM is established through the combined effects of permanent magnets, torque windings, and suspension force windings. The magnetomotive force (MMF) can be expressed as

$$\begin{cases} f_m = F_m \cos(\omega t - p_m\theta - \mu) \\ f_s = F_s \cos(\omega t - p_s\theta - \lambda) \end{cases} \tag{1}$$

where F_m and μ are the fundamental component and initial phase angle of the MMF of the torque winding and PM; F_s and λ are the fundamental component and initial phase angle of the MMF of the suspension force winding; ω is the current frequency; θ is the spatial angle between any point in the air gap and the x axis. The air gap flux density can be written as

$$\begin{cases} B_m(\theta,t) = \Lambda(\theta) f_m(\theta,t) \\ B_s(\theta,t) = \Lambda(\theta) f_s(\theta,t) \end{cases} \tag{2}$$

where $\Lambda(\theta)$ is the air gap permeability per unit area. The total air gap flux density can be expressed as

$$\begin{aligned} B_\delta(\theta,t) =& B_m \cos(\omega t - p_m\theta - \mu) \\ &+ B_s \cos(\omega t - p_s\theta - \lambda) \end{aligned} \tag{3}$$

According to Maxwell tensor method, the electromagnetic force on the rotor surface can be expressed as

$$dF(\theta) = \frac{B_\delta^2(\theta,t) \cdot dS}{2\mu_0} = \frac{B_\delta^2(\theta,t)}{2\mu_0}(lrd\theta) \tag{4}$$

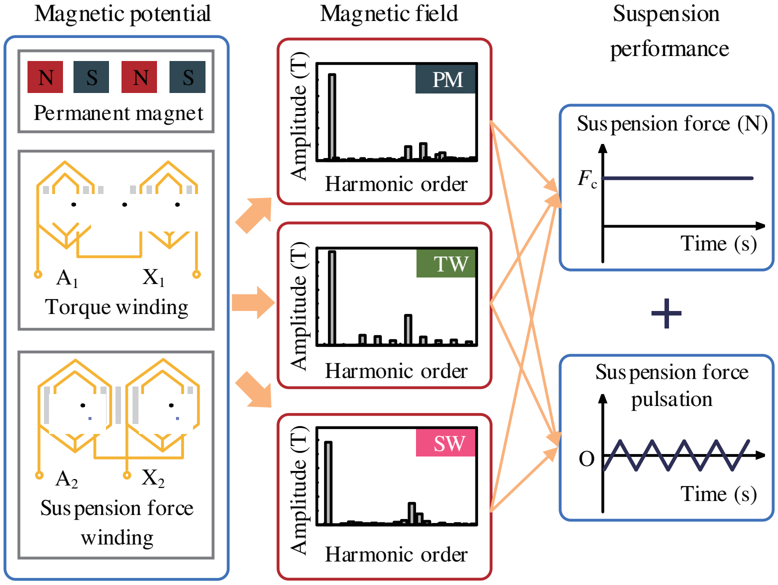

FIGURE 2. Effect of harmonic magnetic field on suspension force performance.

where l is the effective core length of the motor, and r is the rotor radius.

By substituting (3) into (4) and conducting orthogonal decomposition, the electromagnetic force component in the x and y axes can be expressed as

$$\begin{cases} dF_x(\theta,t) = dF(\theta,t)\cdot\cos\theta = \dfrac{B_\delta^2(\theta,t)Rl\cos\theta d\theta}{2\mu_0} \\ dF_y(\theta,t) = dF(\theta,t)\cdot sin\theta = \dfrac{B_\delta^2(\theta,t)Rl\sin\theta d\theta}{2\mu_0} \end{cases} \tag{5}$$

Integrating (5) along the circumference, the expression for the suspension force is

$$F_{mag} = \sqrt{(F_x)^2 + (F_y)^2} = \frac{\pi RlB_MB_S}{2\mu_0} \tag{6}$$

$$\begin{cases} F_x = \dfrac{\pi RlB_MB_S}{2\mu_0}cos(\mu-\lambda) \\ F_y = \dfrac{\pi RlB_MB_S}{2\mu_0}sin(\mu-\lambda) \end{cases} \tag{7}$$

The stable suspension force of the PMa-BSynRM can be achieved by superimposing magnetic fields generated by the torque winding and suspension force winding, as demonstrated in (6). Furthermore, (7) reveals that the initial phase angle of the magnetic field influences both the x-axis and y-axis suspension forces, thereby altering the direction of the combined suspension force. Consequently, precise control over both magnitude and phase of the suspension winding current enables directional controllability of suspension forces.

2.3. Modeling of the Suspension Force

The mathematical model of the suspension force of PMa-BSynRM under ideal conditions is given in the previous section. However, in practical cases, the stator slots and rotor barrier can result in many harmonic magnetic fields in the air gap of the PMa-BSynRM. These harmonic magnetic fields superposition with each other will produce a constant suspension force or suspension force pulsation, as shown in Fig. 2, and then affect the suspension performance of PMa-BSynRM. Therefore, this section analyzes the conditions under which suspension force or suspension force pulsation is generated by magnetic field superposition, which has guiding significance for the subsequent optimization of PMa-BSynRM suspension force performance.

For the stator winding MMF, due to the stator slot, the air gap contains harmonic MMF, and the harmonic MMF generated by the torque winding and suspension force winding can be expressed as

$$\begin{cases} f_{mv} = \sum F_{mv}\cos(\omega t - vp_m\theta - \mu_v) \\ f_{sv} = \sum F_{sv}\cos(\omega t - vp_s\theta - \lambda_v) \end{cases} \tag{8}$$

where $v = 6k+1$, $k = \pm1, \pm2 \ldots$

Since the magnetic field of PMa-BSynRM is non-sinusoidal, the magnetic potential of PM is also composed of a series of harmonic MMF

$$f_{vPM} = \sum F_{\eta PM}\cos(\eta\omega t - \eta p_m\theta) \tag{9}$$

where $\eta = 2k+1$, $k = 0, 1, 2\ldots$

The rotor surface of PMa-BSynRM is smooth, but because the stator is slotted, the air gap permeability can be expressed as

$$\Lambda(\theta,t) = \Lambda_0 + \sum_{k=1,2,3}^{\infty}\Lambda_k\cos(kZ\theta) \tag{10}$$

Combined with (8) to (10), the air gap flux density expression of PMa-BSynRM can be written as

$$\begin{aligned} B(\theta,t) =& f(\theta,t)\Lambda(\theta,t) \\ =& [f_m(\theta,t)+f_s(\theta,t)]\cdot\Lambda_0 \\ &+ f_{mv}(\theta,t)+f_{sv}(\theta,t)]\cdot\Lambda_0 \\ &+ [f_m(\theta,t)+f_s(\theta,t)]\cdot\sum_{k=1,2,3}^{\infty}\Lambda_k\cos(kz\theta) \end{aligned} \tag{11}$$

It can be seen from (11) that the internal harmonic magnetic field of PMa-BSynRM is very complex. To make the conclusion universal, the electromagnetic force generated on the rotor surface under the action of any two radial magnetic fields, $B_{\delta a}(\theta,t)$ and $B_{\delta b}(\theta,t)$, is first assumed to be analyzed.

$$\begin{cases} B_{\delta\alpha}(\theta,t) = B_\alpha\cos(p_\alpha\theta-\omega_\alpha t-\varphi_\alpha) \\ B_{\delta\beta}(\theta,t) = B_\beta\cos(p_\beta\theta-\omega_\beta t-\varphi_\beta) \end{cases} \tag{12}$$

The electromagnetic force generated by the coupling of these two magnetic fields on the rotor can still be obtained by the Maxwell tensor method.

$$\begin{aligned} F_{\delta\alpha\beta} =& \int_0^{2\pi}\frac{[B_{\delta\alpha}(\theta,t)+B_{\delta\beta}(\theta,t)]^2}{2\mu_0}dS \\ =& \frac{RlB_{\delta\alpha}B_{\delta\beta}}{4\mu_0}\int_0^{2\pi}\cos\left[(\omega_\alpha-\omega_\beta)t\right. \\ &\left.+(p_\alpha\pm p_\beta\pm 1)\theta+\varphi_\beta-\varphi_\alpha\right]d\theta \end{aligned} \tag{13}$$

Further, the calculation of (13) can be obtained

$$F_{\delta\alpha\beta} = \begin{cases} \dfrac{\pi RlB_\alpha B_\beta}{2\mu_0}\cos(\varphi_\beta-\varphi_\alpha), \\ \qquad p_\alpha = p_\beta\pm 1 \\ \qquad \omega_\alpha = \omega_\beta \\ \dfrac{\pi RlB_\alpha B_\beta}{2\mu_0}\cos[(\omega_\alpha-\omega_\beta)t+\varphi_\beta-\varphi_\alpha], \\ \qquad p_\alpha = p_\beta\pm 1 \\ \qquad \omega_\alpha \neq \omega_\beta \end{cases} \tag{14}$$

As can be seen from (14), for harmonic magnetic fields with different frequencies and orders of $p_\alpha = p_\beta \pm 1$, a radial electromagnetic force with a frequency of $\omega_\alpha\omega_\beta$ will be generated. This force is part of the resultant suspension force and will cause the suspension force to fluctuate at a frequency consistent with the frequency of the generated electromagnetic force. For the same frequency, a stable radial electromagnetic force is generated when the order $p_\alpha = p_\beta \pm 1$. The direction of the electromagnetic force is determined by the initial phase difference of the two harmonic magnetic fields. Therefore, to enhance the performance of PMa-BSynRM suspension force, reducing the harmonic magnetic field with a pole pairs difference of 1 in the air gap should be prioritized.

3. OPTIMIZATION BY PROCESS

The optimization process of PMa-BSynRM rotor design is presented in this section, and the optimization flowchart is shown in Fig. 3.

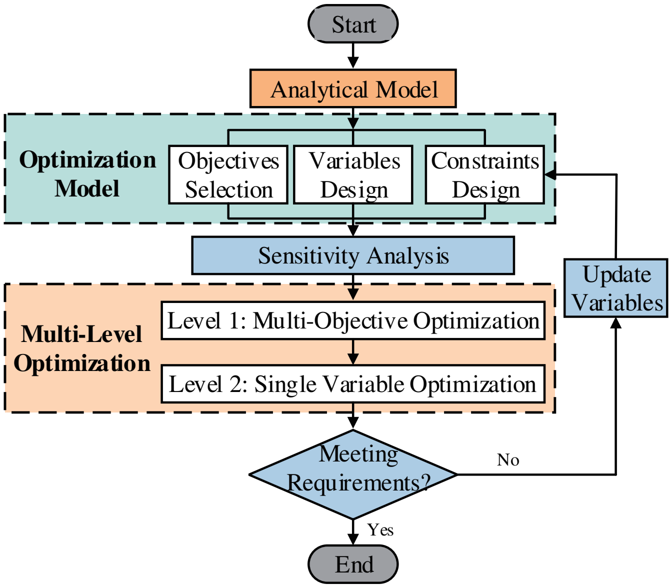

FIGURE 3. Flow chart of optimization process.

3.1. Optimization Model

1) Objectives Selection: For bearingless motor systems, the most fundamental requirement is to achieve high quality torque output while stably suspending the motor rotor. Therefore, the optimization targets are selected as average torque T_{avg}, torque ripple T_{rip}%, average suspension force F_{avg}, and suspension force ripple F_{rip}%.

2) Variables Design: Parameter design is the premise of PMa-BSynRM multi-objective optimization design. For multilayer barriers structure rotor, the traditional design method usually determines the rough structure of the barriers according to experience and then optimizes some parameters. However, in the process of designing PMa-BSynRM rotor structure, it is necessary to consider the influence of rotor structure on the suspension force performance, so it is difficult to learn from the existing rotor structure. Therefore, a method of macroscopic parameters is proposed. The proposed macroscopic parameters have more obvious physical significance, and all parameters can be optimized together, simplifying the difficulty of initial design. It can also lay a foundation for further optimization.

The rotor structure of PMa-BSynRM is shown in Fig. 4. The bridge thickness *bt* is determined by the mechanical strength of the rotor. The barrier is a U-shaped symmetric structure. It can be seen that each magnetic barrier needs five parameters: the inner diameter of the U layer d, the inner thickness of the U layer *it*, the outer thickness of the U layer *ot*, the U layer horizontal width l, and the inclination angle of the U-shaped barrier θ. In order to achieve better initial structural design, some degrees of freedom need to be sacrificed. Let θ represent a fixed value of 45° and let *it* equal *ot*. The thickness of magnets is determined by the magnetic barrier, and the width of magnets l_m is one of

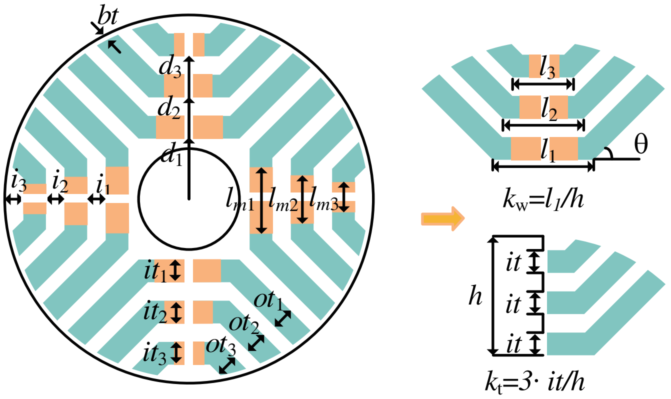

FIGURE 4. Parameters of the PMa-BSynRM rotor structure.

the design variables. The rotor macroscopic parameters design method is as follows.

Step 1: Firstly, d_1 is determined according to the inner diameter of the rotor. In order to give full play to the influence of the magnetic barrier on the anisotropy of the rotor structure, d_1 should be similar in size to rotor inner diameter.

Step 2: Determine l_1; pay attention to the size should not be too large; otherwise, it will lead to different areas of magnetic barrier phase crossing. In order to facilitate the optimization design, the barrier width coefficient k_w is defined: $l_1 = h \times k_w$, where h is the height from the bottom of the barrier to the edge of the rotor, as shown in Fig. 4. After determining l_1, by decreasing factor a, $l_2 = l_1 - a$, $l_3 = l_2 - a$.

Step 3: For the determination of d_2 and d_3, it is necessary to consider the thickness of each layer. The concept of insulation ratio k_t in [19] is used, but the construction method is different for the convenience of calculation, and the thickness of each layer is $it = (R - d_1) \times k_t/3$. The position of the barrier of other layers can be obtained from the recursion relation.

Step 4: The PM is defined by the definition of PM occupancy k_{PM}, permanent magnet length $l_{m1} = l_1 \times k_{PM}$, $l_{m2} = l_{m1} - a$, $l_{m3} = l_{m2} - a$.

3) Constraints Design: The limitation of certain crucial indicators during the process of multi-objective optimization design is imperative to ensure compliance with the specified requirements.

For bearingless motor system, it is necessary to ensure that sufficient suspension force is generated to support stable suspension operation of the rotor. Considering that the weight of the rotor is 3.1 kg, that is, the gravity force on the rotor is 31 N. According to the FEA, the unstable stiffness value in y-direction is 110.87 N/m, and the maximum unbalanced magnetic pull is 166.31 N. Therefore, combined with the design experience, the target value of suspension force is set as 250 N.

In addition, the error angle of the suspension force must be guaranteed within an acceptable range. The angle between the suspension force vector and interference force is called error angle. If the error angle is greater than 17°, the phase margin of the closed-loop system will reach $-180°$, resulting in system instability [20]. Therefore, the PMa-BSynRM suspension force system should meet the following restrictions.

$$\begin{cases} F_y \geq 250 \\ \phi_{error} < 15 \end{cases} \tag{15}$$

3.2. Sensitivity Calculation

To narrow the design space, the sensitivity analysis is required before optimization. The sensitivity index of the optimization parameters can be expressed as [15]:

$$S_{ni}^{m} = \left.\frac{\partial f}{\partial z_i}\right|_{NOP} \frac{z_i}{f} \approx \frac{\Delta f/f}{\Delta z_i/z_i} \tag{16}$$

where z_i represents the design variables, and f is the function of optimization objectives.

According to (16), the sensitivity index calculation results are given in Fig. 5. According to the traditional multi-objective optimization algorithm, 3–4 parameters with the highest sensitivity are usually selected for multi-objective optimization. However, for permanent magnet assisted reluctance rotors, the traditional optimization methods are difficult to achieve good results due to the complex structure and numerous parameters. In the following section, the results of multi-objective optimization based on traditional methods and macro-parameters will be compared and analyzed.

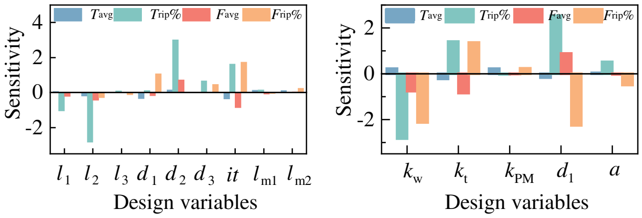

FIGURE 5. Results of sensitivity indices of the design variables to each optimization objective.

3.3. Multi-Objective Optimization

After constructing macroscopic parameters, although the reduction in parameters simplifies the initial structural design process, it also limits the design freedom and may not yield a globally optimal solution. Therefore, a hierarchical optimization approach is employed by combining multi-objective optimization with single objective optimization.

Although the torque component of PMa-BSynRM is dominated by reluctance torque, the improper design of PMs has a great influence on the harmonic content of air-gap magnetic field. Therefore, firstly, k_1, k_2, and k_3 belong to level 1, whose values can be obtained by the RSM. According to the optimization results of level 1, univariate optimization is carried out on the content of each layer of PMs.

1) DOE and RSM: Reasonable design of experiments (DOE) is necessary to effectively select the FEA results to establish the RSM, and the following requirements should be met: 1) Provide a reasonable distribution of data points and other information over the whole area of the study. 2) Provide internal error

estimators. 3) Provide correct estimates of model coefficients. 4) Provide appropriate robustness to outliers or missing data. 5) Ensure the simplicity of model parameter calculation.

Box-Behnken design (BBD) is used in this experiment. BBD is a three-level design of response surface design combined with factorial design and incomplete block design. Its important characteristic is to estimate first-order, second-order, and first-order polynomials with interaction terms with less experimental times, which is an efficient response surface design. Taking macroscopic parameter design as an example, the corresponding levels of each factor in this design are shown in Table 1.

TABLE 1. Levels of significant design variables.

Control Factor	-1	0	$+1$
A: k_w	0.8	0.9	1
B: k_t	0.4	0.5	0.6
C: a (mm)	2	4.5	7
D: d_1 (mm)	12	13	14

The macro parameter optimization variables are k_w, k_t, a, and d_1, and a total of 29 groups of experiments need to be done using BBD for 4 factors and 3 levels experiment. The 29 groups of data are analyzed in the FEM, and then the corresponding relationship between the optimization objective and variables are fitted by RSM. The polynomial models that RSM is often used to fit include linear model, second-order model, and third-order model. The expressions for the RSM are

$$\hat{y}=\sum_{i=1}^{q}\beta_i x_i \tag{17}$$

$$\hat{y}=\sum_{i=1}^{q}\beta_i x_i+\sum_{i<j}^{q-1}\sum_{j}^{q}\beta_{ij}x_i x_j \tag{18}$$

$$\hat{y}=\sum_{i=1}^{q}\beta_i x_i+\sum_{i<j}^{q-1}\sum_{j}^{q}\beta_{ij}x_i x_j$$
$$+\sum_{i<j}^{q-1}\sum_{j}^{q}\delta_{ij}x_i x_j(x_i-x_j)+\sum_{i<j}^{q-2}\sum_{j<k}^{q-1}\sum_{k}^{q}\beta_{ijk}x_i x_j x_k \tag{19}$$

It is very important to select the appropriate model for multi-objective optimization based on RSM. If the model is not suitable, it not only will fail to predict accurately but also may cause serious errors. The choice of RSM can be judged by analysis of variance. The more the correlation coefficient R^2 is close to 1, the smaller the error between the fitted model and the actual model will be. Generally, improving the model order can improve R^2. Finally, T_{avg} and F_{avg} are selected as quadratic models, and T_{rip}% and F_{rip}% as linear models. According to the ANOVA, the R^2 values of four models are all higher than 0.9.

2) DPCA: After RSM is used to obtain the equation, multi-objective optimization algorithm is needed to ensure that each optimization objective has better performance. NSGA-II and MOPSO are the most commonly used multi-objective optimization algorithms. NSGA-II passes information through genetic operators, and MOPSO guides other particles through globally optimal examples. The two algorithms have their own advantages: NSGA-II has strong searching ability, and MOPSO has fast convergence. This paper combines the two algorithms to make full use of their respective advantages. The algorithm flow is shown in Fig. 6.

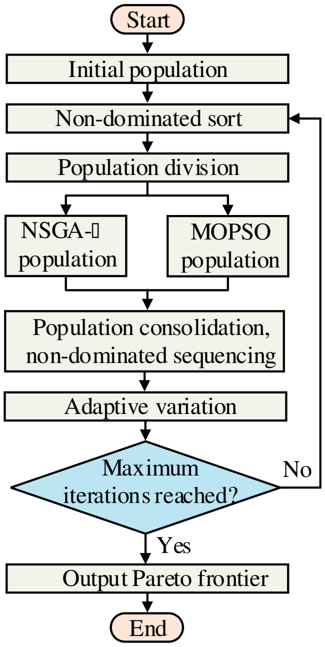

FIGURE 6. Flowchart of the DPCA.

The DPCA is based on the non-dominated ordering of NSGA-II, which divides the initial, non-dominated ordering population into two halves. The top half of the population with good Pareto rank is the elite population, and NSGA-II's strong searching ability is used to explore other Pareto solution sets in the region and find out the non-dominant solution. The lower half of the group with poor Pareto level uses MOPSO algorithm to learn the elite population.

In order to verify the effectiveness of the DPCA algorithm, ZDT1, ZDT2, ZDT3, and ZDT4 of ZDT series test functions [21] are selected as test functions in this paper for comparative analysis. The Pareto frontiers (PFs) of these test functions are known and have different shapes, which provides the necessary conditions for quantifying the performance of the algorithm. The PFs obtained by using the DPCA algorithm, MOPSO algorithm, and NSGA-II algorithm on the ZDT test function are shown in Fig. 7. The population is set to 150, the maximum archive size set to 100, and the maximum iteration set to 200. When solving ZDT1, ZDT2, and ZDT3 problems, the optimized solution distribution of the proposed algorithm is well distributed, and the whole PF of the problem can be covered successfully. For the ZDT4 problem, the DPCA overcomes the shortcoming that the traditional algorithm cannot converge quickly to the true PF. The solution set generated

TABLE 2. Index of optimal solution of ZDTs series functions obtained through different algorithms.

Test Function	Evaluation Indicator	Algorithm		
		DPCA	MOPSO	NSGA-II
ZDT1	IGD	3.6752E-03	8.3109E-03	3.4481E-03
	GD	3.2851E-04	7.2531E-04	1.3198E-04
ZDT2	IGD	4.4308E-03	6.0469E-03	5.5800E-03
	GD	2.6570E-03	4.4328E-04	3.4207E-04
ZDT3	IGD	4.2971E-03	1.4091E-02	9.1634E-03
	GD	2.2206E-04	7.1132E-04	1.1492E-03
ZDT4	IGD	3.6510E-03	5.2800E-01	1.6416E-00
	GD	5.2198E-05	4.5351E-02	1.4987E-01

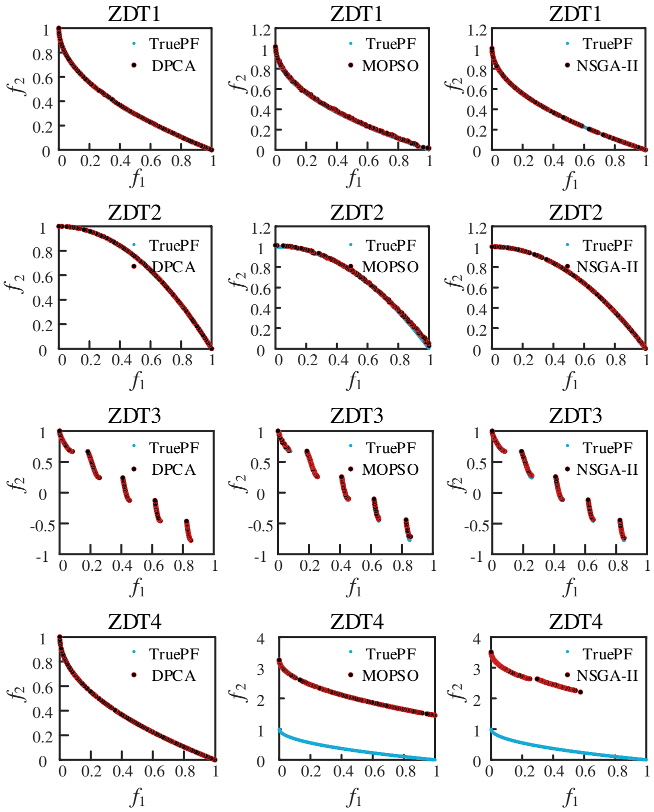

FIGURE 7. Optimal solution set distribution figure of different algorithms obtained on test functions ZDT1, ZDT2, ZDT3 and ZDT4.

by DPCA successfully converges to the true PF, and the solution set is uniformly distributed.

To further quantitatively elaborate the practical benefits brought by the proposed method, the generation distance (GD) and inverted generational distance (IGD) values of the three algorithms on 4 multi-objective test problems are listed in Table 2. GD and IGD are often used as evaluation indexes of multi-objective optimization algorithms, reflecting the ability of algorithms to find true PFs [22]. To reduce the influence of random factors in the multi-objective optimization algorithm on the performance analysis of the algorithm, the values listed in Table 2 are the average of the statistical results of 30 independent runs of the same algorithm on the same test problem. It can be seen from Table 2 that only IGD and GD in ZDT1 of DPCA are slightly inferior to NSGA-II, while IGD and GD indexes in ZDT2, ZDT3, and ZDT4 are significantly superior to the other three algorithms. DPCA has a clear advantage on the ZDT series benchmark problem and shows superior performance on more objective problems. Of course, the algorithm cannot be expected to get the best value on every test problem.

The PFs of the four optimization objectives are shown in Fig. 8. The obtained Pareto optimal solution can be divided into four regions: A, B, C, and D. Region A has small torque ripple, suspension force ripple, and large torque, but the suspension force is too small. Although the suspension force in region D is very large, the other three indexes are not as good as those in other regions. Considering that although the suspension force in area B is not as good as that in area C, the other three indexes are all better than that in area C, so the point in area B is finally selected as the final result.

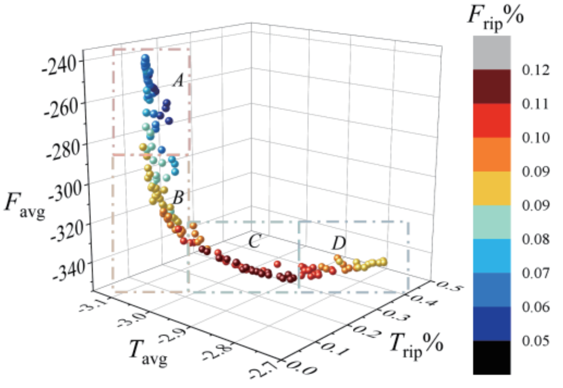

FIGURE 8. Pareto frontier.

4. VERIFICATION

4.1. Simulations Results

The proposed method is verified by the FEM. In the proposed macroscopic parameters, k_w and k_t determine the overall shape of the magnetic barrier. Firstly, the performance under different k_w and k_t values is simulated to verify the rationality of the selection range in Table 1.

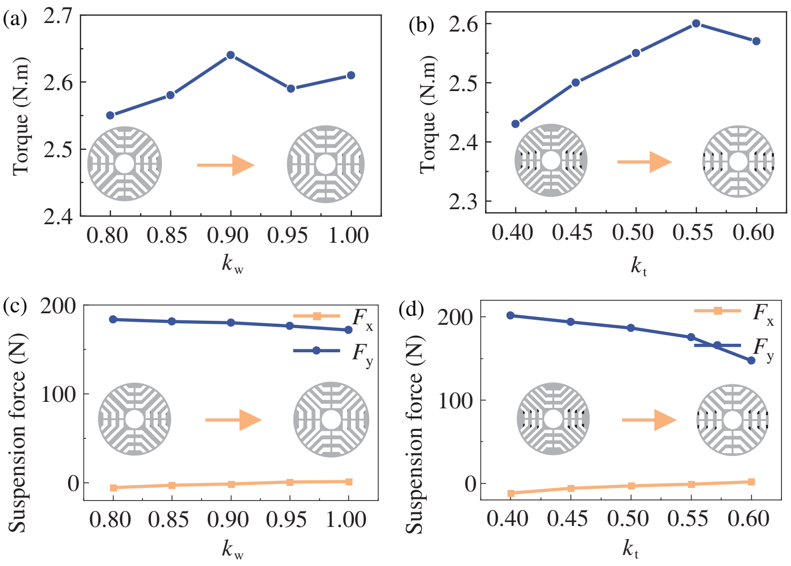

FIGURE 9. PMa-BSynRM performance under different macroscopic parameters. (a) The relationship between T_{avg} and k_w. (b) The relationship between T_{avg} and k_t (c) The relationship between F_{avg} and k_w. (d) The relationship F_{avg} and k_t.

The selection of the barrier shape parameter plays a crucial role in PMa-BSynRM, as reluctance torque constitutes the primary component of the overall torque. In Figs. 9(a) and (b), it can be seen that with the increase of k_w and k_t, the torque rises first and then decreases, which is due to the increase in the difference between the inductances of d and q axes, and the saturation of the rotor magnetic circuit caused by excessive magnetic barrier.

The variation trend of suspension force performance with macroscopic parameters is shown in Figs. 9(c) and (d). As for the performance of suspension force, it is not sensitive to the shape of magnetic barrier because it mainly depends on the superposition of magnetic fields of two sets of windings in the stator. However, when the barrier part is larger, it will inevitably lead to a larger rotor reluctance, resulting in a substantial decrease in suspension force. Its variation trend is not the same as the torque. Therefore, it is necessary to rely on multi-objective optimization algorithm to achieve the compromise of two kinds of performance.

In order to verify whether the macroscopic parameters designed in this paper are reasonable. The multi-objective optimization design method based on macroscopic parameters is compared with the traditional method. The traditional method selects several parameters with the highest sensitivity among many parameters for optimization. According to the previous sensitivity analysis, the optimization parameters selected in the traditional method are l_1, l_2, d_2, and it.

The suspension force and torque performance of PMa-BSynRM after optimization are shown in Fig. 10 and Fig. 11. Compared with the initial motor, based on the optimization results of the traditional method, F_{avg} is increased by 9%, $F_{rip}\%$ reduced by 21%, T_{avg} reduced by 1%, and $T_{rip}\%$ reduced by 39%. The optimization results based on the proposed method show that F_{avg} is decreased by 3%, $F_{rip}\%$ decreased by 51%, T_{avg} increased by 9%, and $T_{rip}\%$ decreased by 74%. The $T_{rip}\%$ and $F_{rip}\%$ based on proposed method are significantly reduced, and only the suspension force falls slightly, because when the final optimization results are chosen, the lower torque ripple and suspension force ripple are preferred. In addition, it can be seen that the maximum suspension force error angles of the initial motor, the traditional method, and the

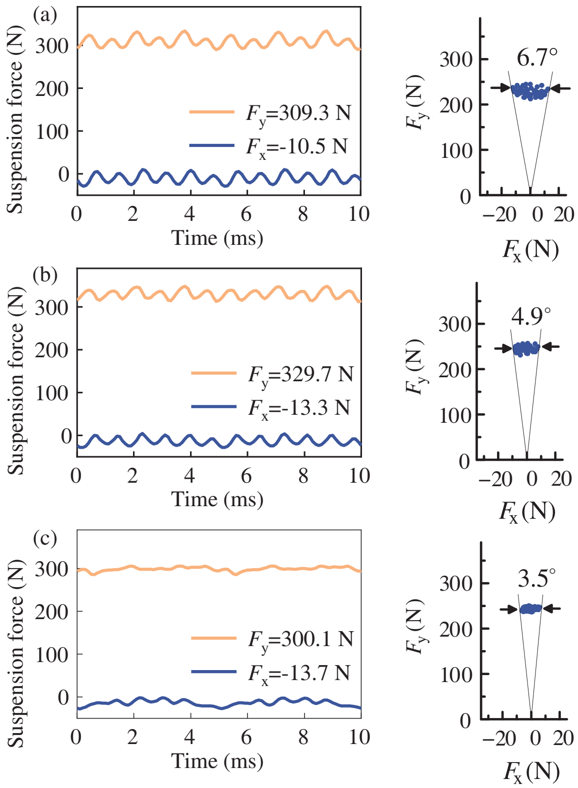

FIGURE 10. The radial suspension force waveforms in the x- and y-direction. (a) Initial motor. (b) Optimization by traditional method. (c) Optimization by proposed method.

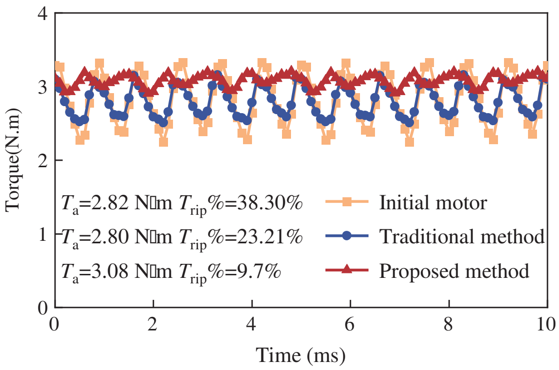

FIGURE 11. Comparison of torque.

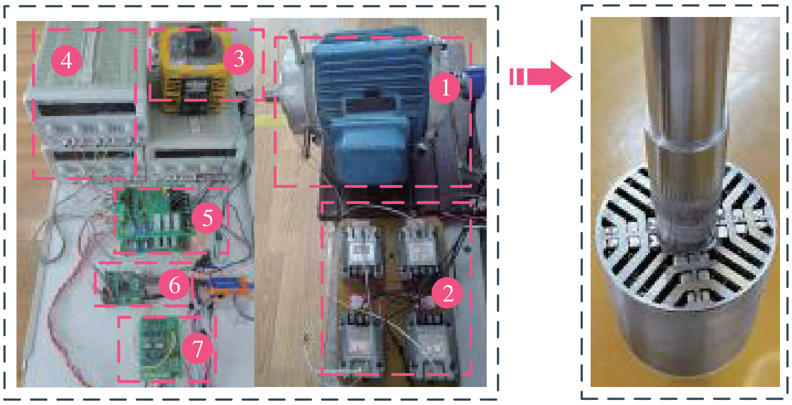

FIGURE 12. Experiment platform, (1) prototype, (2) eddy current sensor. (3) AC voltage regulator, (4) DC power supply, (5) power driver board, (6) DSP board, (7) interface circuit board.

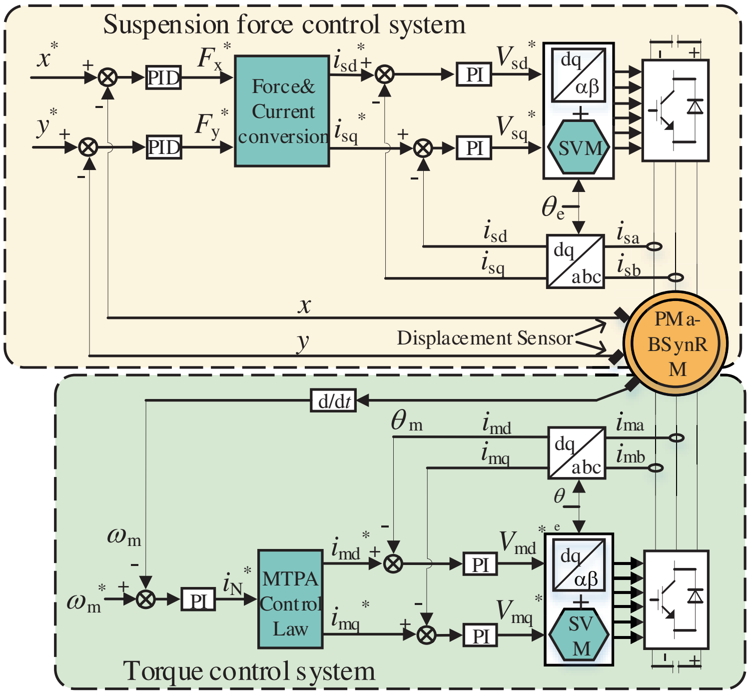

FIGURE 13. Vector control block diagram of the PMa-BSynRM.

proposed method are 6.7°, 4.9°, and 3.5°, respectively, which also proves the rationality of the optimization.

4.2. Experimental Results

The prototype of the optimal rotor is manufactured. The rotor radial displacements are measured by eddy current sensors, and the experimental platform takes TMS320F28335 as the core. The experimental platform is shown in Fig. 12. One end of the PMa-BSynRM is supported by a three-degree-of-freedom aligning ball bearing, and the other end is equipped with an auxiliary bearing. There is a 0.25 mm auxiliary mechanical bearing clearance between the auxiliary bearing and the shaft, which can realize two-degree-of-freedom suspension. In the experiment, torque control system adopts maximum torque per ampere (MTPA) control. Suspension force control system adopts displacement current double closed loop control. The control system diagram is shown in Fig. 13.

The performance of PMa-BSynRM motor is tested and compared with the simulation results. The no-load back EMF waveform of the torque winding is measured, as shown in Fig. 14. The measured back EMF waveform exhibits excellent sinusoidal characteristics and demonstrates strong agreement with the simulation results.

The speed and displacement waveforms of PMa-BSynRM under the acceleration experiment from 1000 r/min to 3000 r/min are shown in Fig. 15. The acceleration process is completed after 130 ms. Due to the coupling of the torque system and the suspension force system, the torque mutation

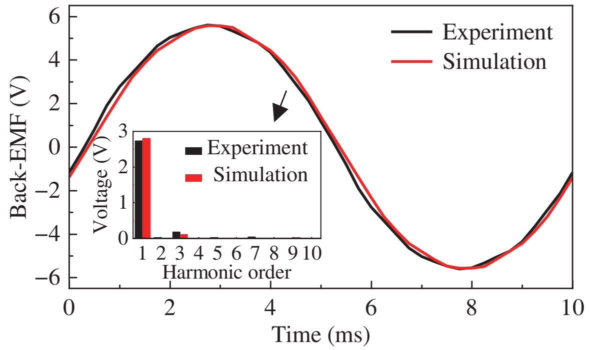

FIGURE 14. No-load back EMF.

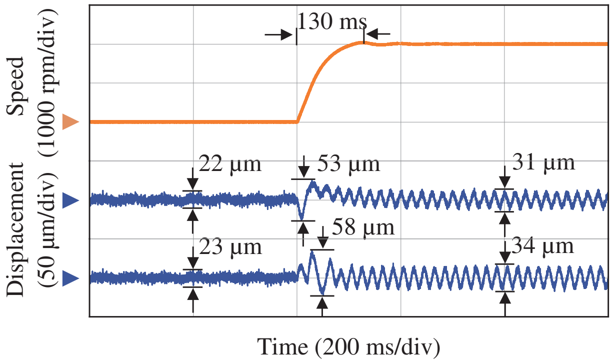

FIGURE 15. Acceleration experiment.

caused by rotor acceleration will cause rotor vibration, and the maximum vibration amplitudes of the rotor in the x- and y-directions are 53 μm and 58 μm, respectively. Due to the influence of unbalanced vibration, the rotor vibration amplitude increases with the increase of speed [7]. When the rotor is 1000 r/min, the rotor vibration amplitudes in x- and y-directions are 22 μm and 23 μm, while when the rotor is 3000 r/min, the rotor vibration amplitudes in x- and y-directions are 31 μm and 34 μm, respectively. It can be seen that during the experiment, the vibration amplitude of the rotor is much smaller than the air gap between the rotor and the auxiliary bearing, and stable suspension operation is realized. When the phase current amplitude is 7.4 A, the output electromagnetic torque of the PMa-BSynRM is shown in Fig. 16. The electromagnetic torque is about 3 N·m, the torque ripple about 10%, and the error between the experimental results and the simulation results is 3.1%, which verifies the correctness of the FEA results.

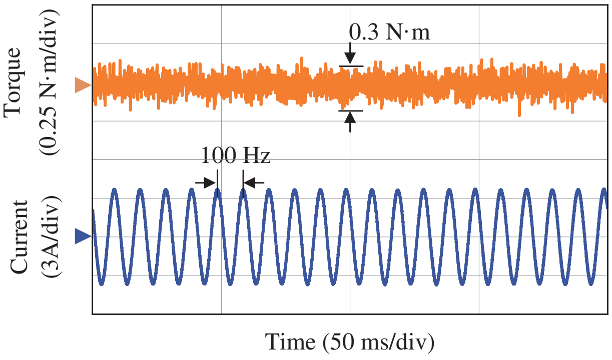

FIGURE 16. Torque experimental result.

5. CONCLUSION

A macroscopic parameters variables design method is proposed for a PMa-BSynRM rotor structure. The influence of parameters on the structure becomes more evident through the construction of macroscopic parameters, aiding in determining the range of optimization variables. This allows for greater participation of parameters in multi-objective optimization algorithms and improves the global nature of the optimization algorithm. On the basis of macroscopic parameters, combining RSM and DPCA, a multi-objective optimization method of PMa-BSynRM is proposed. After multi-objective optimization, the average torque and average suspension force of PMa-BSynRM are improved, and suspension force pulsation and torque pulsation are reduced, indicating significant performance enhancement. Compared with the original motor, the proposed optimization method can reduce F_{rip}% by 51%, T_{rip}% by 74%, and the suspension force error angle is only 3.5°, which is lower than the original error angle of 6.7° and the traditional optimization method error angle of 4.9°. It is shown that the PMa-BSynRM achieves better performance in torque and suspension force system. The experimental results show that the torque of the PMa-BSynRM is about 3 N·m, the pulsation about 10%, and the error of the finite element results is less than 5%, which verifies the rationality of the simulation results. The simulated and experimental results verify the rationality of the parameter design and the effectiveness of the optimization method.

ACKNOWLEDGEMENT

This work was supported by the National Natural Science Foundation of China (62273168, 62303075) and the Postgraduate Research & Practice Innovation Program of Jiangsu Province (KYCX23_3689).

REFERENCES

[1] Pei, T., D. Li, J. Liu, J. Li, and W. Kong, "Review of bearingless synchronous motors: Principle and topology," *IEEE Transactions on Transportation Electrification*, Vol. 8, No. 3, 3489–3502, Sep. 2022.

[2] Beglinger, L., D. Steinert, T. Nussbaumer, and J. Biela, "Concept and design of a bearingless spinfilter," *IEEE/ASME Transactions on Mechatronics*, Vol. 28, No. 4, 1817–1825, Aug. 2023.

[3] Zad, H. S., T. I. Khan, and I. Lazoglu, "Design and analysis of a novel bearingless motor for a miniature axial flow blood pump," *IEEE Transactions on Industrial Electronics*, Vol. 65, No. 5, 4006–4016, May 2018.

[4] Wang, X. and H. Zhu, "Vibration compensation control of BPMSM with dead-time effect based on adaptive neural network band-pass filter," *IEEE Transactions on Power Electronics*, Vol. 37, No. 6, 7145–7155, Jun. 2022.

[5] Yu, Q., X. Cao, X. Deng, T. Zhu, Z. Deng, and C. Liu, "An improved control strategy to reduce torque spikes and ripple for

bearingless switched reluctance motors," *IEEE Transactions on Industrial Informatics*, Vol. 20, No. 4, 5147–5159, Apr. 2024.

[6] Chen, J., Y. Fujii, M. W. Johnson, A. Farhan, and E. L. Severson, "Optimal design of the bearingless induction motor," *IEEE Transactions on Industry Applications*, Vol. 57, No. 2, 1375–1388, Apr. 2021.

[7] Mao, B. and H. Zhu, "Unbalance vibration suppression control of PMa-BSynRM based on total least square adaptive filtering algorithm," *IEEE Journal of Emerging and Selected Topics in Power Electronics*, Vol. 11, No. 6, 5798–5808, Dec. 2023.

[8] Xu, M., G. Liu, Q. Chen, J. Ji, and W. Zhao, "Design and optimization of a fault tolerant modular permanent magnet assisted synchronous reluctance motor with torque ripple minimization," *IEEE Transactions on Industrial Electronics*, Vol. 68, No. 9, 8519–8530, Sep. 2021.

[9] Gallicchio, G., M. D. Nardo, M. Palmieri, A. Marfoli, M. Degano, C. Gerada, and F. Cupertino, "High speed permanent magnet assisted synchronous reluctance machines — Part I: A general design approach," *IEEE Transactions on Energy Conversion*, Vol. 37, No. 4, 2556–2566, Dec. 2022.

[10] Di Nardo, M., G. Gallicchio, M. Palmieri, A. Marfoli, M. Degano, C. Gerada, and F. Cupertino, "High speed permanent magnet assisted synchronous reluctance machines — Part II: Performance boundaries," *IEEE Transactions on Energy Conversion*, Vol. 37, No. 4, 2567–2577, Dec. 2022.

[11] Sun, X., Z. Shi, and J. Zhu, "Multiobjective design optimization of an IPMSM for EVs based on fuzzy method and sequential Taguchi method," *IEEE Transactions on Industrial Electronics*, Vol. 68, No. 11, 10 592–10 600, Nov. 2021.

[12] Gu, J., W. Hua, W. Yu, Z. Zhang, and H. Zhang, "Surrogate model-based multiobjective optimization of high-speed PM synchronous machine: Construction and comparison," *IEEE Transactions on Transportation Electrification*, Vol. 9, No. 1, 678–688, Mar. 2023.

[13] Zhu, H., S. Shen, and X. Wang, "Multiobjective optimization design of outer rotor coreless bearingless permanent magnet synchronous motor," *IEEE Journal of Emerging and Selected Topics in Power Electronics*, Vol. 9, No. 5, 5489–5498, Oct. 2021.

[14] Wu, M., H. Zhu, H. Zhang, and W. Zhang, "Modeling and multi-level design optimization of an AC–DC three-degree-of-freedom hybrid magnetic bearing," *IEEE Transactions on Industrial Electronics*, Vol. 70, No. 1, 233–242, Jan. 2023.

[15] Hua, Y., H. Zhu, and Y. Xu, "Multi-objective optimization design of bearingless permanent magnet synchronous generator," *IEEE Transactions on Applied Superconductivity*, Vol. 30, No. 4, 1–5, Jun. 2020.

[16] Sun, X., Z. Shi, G. Lei, Y. Guo, and J. Zhu, "Multi-objective design optimization of an IPMSM based on multilevel strategy," *IEEE Transactions on Industrial Electronics*, Vol. 68, No. 1, 139–148, Jan. 2021.

[17] Diao, K., X. Sun, G. Lei, Y. Guo, and J. Zhu, "Multiobjective system level optimization method for switched reluctance motor drive systems using finite-element model," *IEEE Transactions on Industrial Electronics*, Vol. 67, No. 12, 10 055–10 064, Dec. 2020.

[18] Cai, J., Z. Q. Deng, R. Y. Qi, Z. Y. Liu, and Y. H. Cai, "A novel BVC-RBF neural network based system simulation model for switched reluctance motor," *IEEE Transactions on Magnetics*, Vol. 47, No. 4, 830–838, Apr. 2011.

[19] Moghaddam, R.-R. and F. Gyllensten, "Novel high-performance SynRM design method: An easy approach for a complicated rotor topology," *IEEE Transactions on Industrial Electronics*, Vol. 61, No. 9, 5058–5065, Sep. 2014.

[20] Chiba, A., T. Fukao, O. Ichikawa, M. Oshima, M. Takemoto, and D. G. Dorrell, *Magnetic Bearings and Bearingless Drives*, Elsevier, 2005.

[21] Yi, J., J. Bai, W. Zhou, H. He, and L. Yao, "Operating parameters optimization for the aluminum electrolysis process using an improved quantum-behaved particle swarm algorithm," *IEEE Transactions on Industrial Informatics*, Vol. 14, No. 8, 3405–3415, Aug. 2018.

[22] Lin, F., J. Zeng, J. Xiahou, B. Wang, W. Zeng, and H. Lv, "Multiobjective evolutionary algorithm based on nondominated sorting and bidirectional local search for big data," *IEEE Transactions on Industrial Informatics*, Vol. 13, No. 4, 1979–1988, Aug. 2017.